



# Effects of Fe dopants and residual carbonates on the catalytic activities of the perovskite-type $\text{La}_{0.7}\text{Sr}_{0.3}\text{Co}_{1-x}\text{Fe}_x\text{O}_3$ $\text{NO}_x$ storage catalyst

Ai-Jing Ma<sup>a</sup>, Shao-Zeng Wang<sup>a</sup>, Cheng Liu<sup>a,b</sup>, Hui Xian<sup>a,c</sup>, Quan Ding<sup>a,b</sup>, Li Guo<sup>a,b</sup>, Ming Meng<sup>a,b</sup>, Yi-Sheng Tan<sup>d</sup>, Noritatsu Tsubaki<sup>e</sup>, Jing Zhang<sup>f</sup>, Li-Rong Zheng<sup>f</sup>, Xin-Gang Li<sup>a,b,\*</sup>

<sup>a</sup> Tianjin Key Laboratory of Applied Catalysis Science & Technology, School of Chemical Engineering & Technology, Tianjin University, Tianjin 300072, PR China

<sup>b</sup> The Synergetic Innovation Center of Chemistry and Chemical Engineering of Tianjin, Tianjin 300072, PR China

<sup>c</sup> Pei-Yang Distillation Engineering Limited Company, Tianjin 300072, PR China

<sup>d</sup> State Key Laboratory of Coal Conversion, Institute of Coal Chemistry, Chinese Academy of Science, Taiyuan 030001, PR China

<sup>e</sup> Department of Applied Chemistry, School of Engineering, University of Toyama, Gofuku 3190, Toyama city, Toyama 930-8555, Japan

<sup>f</sup> Institute of High Energy Physics, Chinese Academy of Sciences, Beijing 100049, PR China

## ARTICLE INFO

### Article history:

Received 28 October 2012

Received in revised form 5 May 2013

Accepted 11 June 2013

Available online 20 June 2013

### Keywords:

Perovskite

Fe dopant

Carbonates

$\text{NO}_x$  storage

Sulfur tolerance

## ABSTRACT

Herein, we reported the  $\text{NO}_x$  storage capacity, NO oxidation ability and sulfur resistance of the  $\text{La}_{0.7}\text{Sr}_{0.3}\text{CoO}_3$ -based perovskite-type catalysts. NO could be readily oxidized to  $\text{NO}_2$  with around 83% of NO-to- $\text{NO}_2$  conversion at 300 °C over the perovskite. After sulfation, the NSC of the  $\text{La}_{0.7}\text{Sr}_{0.3}\text{CoO}_3$  catalyst calcined in static air decreased 58.0%. Nevertheless, a significant improvement of the sulfur tolerance could be achieved through partial substitution of Co with Fe cations, as well as calcination in flowing air. The NSC of the pre-sulfated  $\text{La}_{0.7}\text{Sr}_{0.3}\text{Co}_{0.8}\text{Fe}_{0.2}\text{O}_3$  catalyst maintained 360.7  $\mu\text{mol/g}$  and dropped only 6.4% as compared with the fresh one. The XPS results confirmed the presence of  $\text{Fe}_2(\text{SO}_4)_3$  in the sulfated  $\text{La}_{0.7}\text{Sr}_{0.3}\text{Co}_{0.8}\text{Fe}_{0.2}\text{O}_3$  catalyst. The EXAFS results further revealed that the formation of  $\text{Fe}_2(\text{SO}_4)_3$  in the perovskite inhibited the sulfation of neighboring strontium from the viewpoint of the local atomic level. These findings strongly suggest that the  $\text{La}_{0.7}\text{Sr}_{0.3}\text{Co}_{0.8}\text{Fe}_{0.2}\text{O}_3$  perovskite is a possible  $\text{NO}_x$  absorber used for aftertreatment systems upon lean-burn engines with the advantages of the excellent NO oxidation ability,  $\text{NO}_x$  storage capacity and the high sulfur tolerance.

© 2013 Elsevier B.V. All rights reserved.

## 1. Introduction

During the past years, the emission control of  $\text{CO}_2$  from mobile vehicles has attracted more attention owing to its great contributions to global warming. One of the most efficient ways is to utilize the lean-burn technology which can suppress greenhouse gas emissions and offer superior fuel economy efficiencies, as well [1,2]. However, under such a condition, nitrogen oxide ( $\text{NO}_x$ , including NO and  $\text{NO}_2$ ) emission is hardly controlled because the traditional three-way catalysts (TWCs) cannot efficiently remove  $\text{NO}_x$  in excessive  $\text{O}_2$  atmospheres [3]. Lean  $\text{NO}_x$  Traps (LNT) (also named  $\text{NO}_x$  storage-reduction, i.e. NSR) technique, which was first proposed by Toyota Company [4], is regarded as one of promising methodologies to remove  $\text{NO}_x$  from lean-burn engines. It does not need any additional reductant generating equipment or infrastructure, e.g. urea tanks used in the  $\text{NH}_3$  Selective Catalytic Reduction ( $\text{NH}_3$ -SCR) systems [5,6]. Undoubtedly, the application of the LNT technique

will suppress the volumes of the exhaust aftertreatment system, especially for diesel cars [7].

The conventional LNT catalysts consist of three kinds of components [8,9]: (1) noble metal (e.g. Pt, Rh, Pd, or their alloys); (2) storage component (e.g. BaO,  $\text{K}_2\text{O}$  or  $\text{Li}_2\text{O}$ ); (3) the support (e.g.  $\text{Al}_2\text{O}_3$  or  $\text{TiO}_2\text{-ZrO}_2$ ). Regarding the Pt/BaO/ $\text{Al}_2\text{O}_3$  model catalyst [10,11], the  $\text{NO}_x$  storage-reduction process can be described as follows: During a long lean-burn period, NO is firstly oxidized to  $\text{NO}_2$  on the Pt sites and then stored on the neighboring BaO sites in the form of nitrites or nitrates; during a short fuel-rich period, the stored  $\text{NO}_x$  can be readily released and then reduced to  $\text{N}_2$  on the adjacent Pt sites by reductants (e.g. CO, hydrocarbons and  $\text{H}_2$ ) [12]. Through the successive alternations between the lean-burn and fuel-rich operations,  $\text{NO}_x$  could be efficiently reduced to eco-friendly  $\text{N}_2$ . In spite of its high activity [13], the usage of the noble metals could not be considered as a sustainable solution owing to their limited resources, high price and poor thermal stability. Thus, it is necessary to develop less costly catalysts for the substitution of noble metal based catalysts [14]. Furthermore, the other disadvantage of the present LNT catalysts is the poor sulfur tolerance, which limits their worldwide applications [15–18].

\* Corresponding author. Tel.: +86 22 27892275; fax: +86 22 27892275.  
E-mail address: [xingang.li@tju.edu.cn](mailto:xingang.li@tju.edu.cn) (X.-G. Li).

Since 1970s, the perovskite-type composite metal-oxides in the  $ABO_3$  formula have been regarded as one of promising alternatives for noble metal catalysts in auto-exhaust treatments owing to its controllable redox ability, low cost and highly thermal stability. The modified catalytic activity due to the presence of oxygen vacancies or the abnormal valence of the B site element in perovskite was easily achieved by partial substitution with A and/or B cations [19]. It was reported that the  $LaCoO_3$ -based perovskite catalyst presented a much higher NO oxidation ability than the Pt based LNT catalyst [20,21]. Generally, the perovskites are easily deactivated by sulfur poisoning [22–24], limiting their industrial applications.

It is reported that the addition of  $Fe_2O_3$  to the Pt/BaO/ $Al_2O_3$  catalyst could remarkably enhance its sulfur resistance [25,26]. The iron inhibited the sulfation of barium and only the superficial barium sulfate with small particle sizes was formed. Our group designed a kind of the perovskite-type  $BaFeO_{3-x}NO_x$  storage catalysts, which exhibited an excellent sulfur tolerance. The well dispersed iron element greatly inhibited the formation of  $BaSO_4$  [27–30]. Unfortunately, the relatively lower NO-to- $NO_2$  conversion of the  $BaFeO_{3-x}$  perovskite catalysts [31], which is a key step to a  $NO_x$  storage process [32], limited their applications.

Recently, we first reported a series of the  $La_{1-x}Sr_xCoO_3$  perovskite-type LNT catalysts with a high  $NO_x$  removal performance. They were prepared by the complexation method and calcined at 700 °C in static air. Among these perovskites, the  $La_{0.7}Sr_{0.3}CoO_3$  catalyst displayed the high NO oxidation ability,  $NO_x$  removal efficiency ( $NO_x$  conversion > 71%) and selectivity to  $N_2$  in the alternative lean/rich atmospheres [33]. Loading the perovskite nanoparticles on the mesoporous  $SiO_2$  support could remarkably increase its NSC and improve the stability in reducing atmospheres [34]. Direct addition of Pd to the perovskite could further enhance its  $NO_x$  removal efficiency [35]. It provides a new possibility for the Pt-free LNT catalysts. We also shortly reported that the addition of iron to the  $La_{0.7}Sr_{0.3}CoO_3$  perovskite calcined in static air could enhance its sulfur tolerance that the NSC dropping decreased from 64.2 to 16.6% after sulfation [36], but the experimental improvement on this point was deficient. Besides the perovskite phase itself, the bulk carbonates on the catalysts are readily poisoned by sulfur [24,28,30]. Therefore, it is reasonable to expect that reducing the amount of bulk carbonates and transforming the accumulated bulk carbonates to highly dispersed states in perovskite catalysts may improve their sulfur tolerance.

In this work, we used  $La_{0.7}Sr_{0.3}Co_{1-x}Fe_xO_3$  ( $x=0, 0.2$ ) catalysts as the model perovskite-type catalysts. Compared with our previous work [33,36], the preparation conditions were optimized by increasing the catalyst calcination temperature to 800 °C and calcination in flowing air. These improvements might inhibit the formation of the large bulk carbonates, as well as improving their dispersion. The influence of the Fe-doping and the state of the residual carbonates on the  $NO_x$  storage capacity, NO oxidation ability and the sulfur tolerance of these perovskite catalysts was investigated through the characterizations of the X-ray diffraction (XRD), X-ray photoelectron spectroscopy (XPS),  $H_2$  temperature-programmed reduction ( $H_2$ -TPR), scanning electron microscopy (SEM), FT-IR and extended X-ray absorption fine structures (EXAFS) experiments. Additionally, the possible  $NO_x$  storage mechanism was also discussed in detail.

## 2. Experimental

### 2.1. Catalyst preparation

The  $La_{0.7}Sr_{0.3}Co_{1-x}Fe_xO_3$  ( $x=0$  and 0.2) perovskite catalysts were prepared by a complexation method. Briefly, the required amount of  $La(NO_3)_3 \cdot 6H_2O$ ,  $Sr(NO_3)_2$ ,  $Co(NO_3)_2 \cdot 6H_2O$  and

$Fe(NO_3)_3 \cdot 9H_2O$  was dissolved together in 300 ml of diluted water. Then, citric acid (CA) and ethylene diamine tetraacetic acid (EDTA) were added to the aqueous solution as mentioned above in a molar ratio of “metal cations”:CA:EDTA = 1:1.5:1. Meanwhile, the solution was ultrasonic-treated for 0.5 h to completely dissolve the solid chemicals. Thereafter, the pH value of the aqueous solution was adjusted to around 9.0 with 25%  $NH_3 \cdot H_2O$  solution. The temperature of the aqueous solution was maintained at 80 °C. After vigorous stirring and evaporation, a transparent purple gel was formed, which was then dried at 120 °C overnight. All of the chemicals used here were of analytical grade and purchased from Tianjin Guangfu Technol. Develop. Co. Ltd.

The obtained xerogel precursors were calcined at 300 °C for 4 h in a muffle furnace, and then calcined at 800 °C for 2 h in a pipe furnace in airflow (300 ml/min). The catalysts were denoted as Fe-0-F and Fe-2-F, according to the content of iron at the B sites of the perovskite. For comparison, a part of the xerogel precursors was calcined under the similar conditions, except calcination using the muffle furnace in static air, instead of the pipe furnace in airflow. The obtained catalysts were denoted as Fe-0-S and Fe-2-S, respectively. All of the catalysts were pelletized and crushed to 40–60 mesh for the followed catalytic tests.

### 2.2. Catalyst characterizations

The XRD tests were conducted on an X'Pert Pro rotatory diffractometer, using Cu  $K\alpha$  ( $\lambda=0.15418$  nm) as the radiation source. The X-ray tube was operated at 40 kV and 40 mA. The average crystallite size ( $D$  value) was calculated by Scherrer equation:  $D=0.89\lambda/(B \cos \theta)$ . Here  $\lambda$  is the wavelength of the radiation source (0.15418 nm);  $B$  is the half width of the strongest diffraction peak belonging to the (1 2 1) facet of the perovskite cells, and the value is adopted in the form of radian;  $\theta$  is the diffraction angle of the (1 2 1) facet. During the calculation, the  $D$  value was uncorrected by standard samples, but all of the XRD patterns were collected under the same operating conditions.

The BET surface area was determined by a  $N_2$  physisorption experiment using an automatic gas adsorption system (NOVA 2000, Quantachrome Co.) at 77 K. The sample was outgassed at 350 °C for 10 h prior to the  $N_2$  physisorption experiment.

For the FT-IR experiment, a mixture of the sample and the vacuum-dried IR-grade KBr with a weight ratio of 1:100 was pressed into a disk, and then recorded with a transmission mode using a Nexus FT-IR spectrometer apparatus (Thermo Nicolet Co.) equipped with a MCT detector using 64 scans and a resolution of  $4\text{ cm}^{-1}$  in the range from 400 to 4000  $\text{cm}^{-1}$ .

The surface morphology of the samples was investigated with a Hitachi S-4800 field emission scanning electron microscopy (FE-SEM).

The  $H_2$ -TPR experiments were performed on a TPDRO 1100 SERIES instrument (Thermo-Finnigan Co.) with a thermal conductivity detector (TCD). Before the detection with the TCD, the introduced gas was purified by a  $H_2O$  and  $CO_2$  trap containing CaO and NaOH materials. During the  $H_2$ -TPR operation, the sample (50 mg) was heated from room temperature to 900 °C in the 5%  $H_2/N_2$  flow (20 ml/min) with a rate of 10 °C/min.

The XPS measurements were carried out on a Scienta ESCA-200 spectrometer with an accuracy of 0.3 eV. Al- $K\alpha$  (1486.6 eV) was used as radiation source, and the base pressure was below  $2 \times 10^{-8}$  Pa. The recorded spectra were calibrated by the characteristic binding energy (BE) peak at 284.6 eV belonging to the contaminant carbon in the 1s region.

The EXAFS measurements were collected on the 1W1B beamline of Beijing Synchrotron Radiation Facility (BSRF) (120 mA and 2.5 GeV) with a transmission mode. A Si (1 1 1) double-crystal monochromator was used to reduce the harmonic content in the

source beam. The radial structure functions (RSFs) were achieved by a Fourier transforming method in the range of  $k=2.5\text{--}14\text{Å}^{-1}$  using a Hanning function window.

### 2.3. Catalytic tests

The  $\text{NO}_x$  trapping experiments were carried out with a conventional fixed bed reactor under the atmospheric pressure at  $300^\circ\text{C}$ , which is the optimal temperature that we have reported in our previous work [33]. Before the test, the catalyst (0.5 g) was purged by a  $\text{N}_2$  flow (350 ml/min) to remove  $\text{CO}_2$ ,  $\text{H}_2\text{O}$  and other adsorbed species from atmosphere at  $300^\circ\text{C}$ . Thereafter, a gas mixture of 750 ppm  $\text{NO}$  and 5%  $\text{O}_2$  balanced with  $\text{N}_2$  passed through the loaded catalyst. Here, the space velocity was around  $80,000\text{ h}^{-1}$ . An on-line chemiluminescence  $\text{NO}_x$  analyzer (Model 42i-HL, Thermo Scientific) was occupied to determine the outlet concentration of  $\text{NO}$ ,  $\text{NO}_2$  and  $\text{NO}_x$  in the flow. To check the influence of the space velocity on the  $\text{NO}$  oxidation ability, parts of tests used 0.2 g sample to reach a space velocity of  $200,000\text{ h}^{-1}$ . The composition and flowrate of the feeding gas were the same with other tests. The  $\text{NO}_x$  storage capacity (NSC) and  $\text{NO}$ -to- $\text{NO}_2$  conversion were calculated as the following formula:

$$\begin{aligned}\text{NSC} &= \frac{[\text{NO}_x]_{\text{inlet}} \times V \times t}{(N_0 \times m)} \times \text{storage ratio} \times 10^{-3} \\ &= 28.07 \times t \times \text{storage ratio} (\mu\text{mol/g})\end{aligned}$$

$$\text{NO-to-NO}_2 \text{ conversion (\%)} = \frac{[\text{NO}_2]_{\text{outlet}}}{[\text{NO}_x]_{\text{outlet}}} \times 100\%$$

Here,  $[\text{NO}]$ ,  $[\text{NO}_2]$  and  $[\text{NO}_x]$  is the concentration of  $\text{NO}$ ,  $\text{NO}_2$  and  $\text{NO}_x$  in ppm unit.  $V$  is the flow rate of the inlet gas;  $N_0$  is a constant, i.e.  $22.4\text{ L/mol}$ ;  $m$  is the weight of the catalyst; and storage ratio is the percentage of the stored  $\text{NO}_x$  to the introduced one.

The NSC calculation was taken after the  $\text{NO}_x$  storage process prolonged 60 min. For the calculation of the  $\text{NO}$ -to- $\text{NO}_2$  conversion,  $[\text{NO}_2]_{\text{outlet}}$  and  $[\text{NO}_x]_{\text{outlet}}$  refer to the  $\text{NO}_2$  and  $\text{NO}_x$  concentration, respectively, after the  $\text{NO}_x$  storage process reached a balance.

During the pre-sulfation process, the catalyst was exposed to a gas mixture of 380 ppm  $\text{SO}_2$  balanced with air. The reaction was conducted at  $300^\circ\text{C}$  for 1 h. And the space velocity was around  $20,000\text{ h}^{-1}$ .

## 3. Results and discussion

### 3.1. Structure properties of the $\text{La}_{0.7}\text{Sr}_{0.3}\text{Co}_{1-x}\text{Fe}_x\text{O}_3$ catalysts

The XRD patterns of the  $\text{La}_{0.7}\text{Sr}_{0.3}\text{Co}_{1-x}\text{Fe}_x\text{O}_3$  catalysts are depicted in Fig. 1. It clearly shows that the perovskite structure had been constructed for all of the catalysts. In Fig. 1(b), a weak diffraction peak belonging to the strongest diffraction peak of  $\text{SrCO}_3$  was detected only for the catalysts calcined in static air, i.e. the Fe-0-S and Fe-2-S catalysts. The formation of  $\text{SrCO}_3$  is due to the combustion of CA and EDTA in the precursors. Obviously, the intensity of the diffraction peaks of the perovskite phase in the Fe-0-S and Fe-2-S catalysts is weaker as compared with the catalysts calcined in flowing air. It indicates that the perovskite phase in the catalysts calcined in static air had a relatively poorer crystallinity, and a lot of the bulk carbonates was formed, simultaneously. For the catalysts, whose precursors were calcined in airflow, the carbonate diffraction peak vanished (Fig. 1(b)). It should be noted that the XRD technique can be utilized only for long-range-order crystals with grain sizes usually more than 5 nm, and it is hardly to detect the tiny crystallites. Thus, the disappearance of the carbonate diffraction peak herein indicates that the precursor calcination in flowing

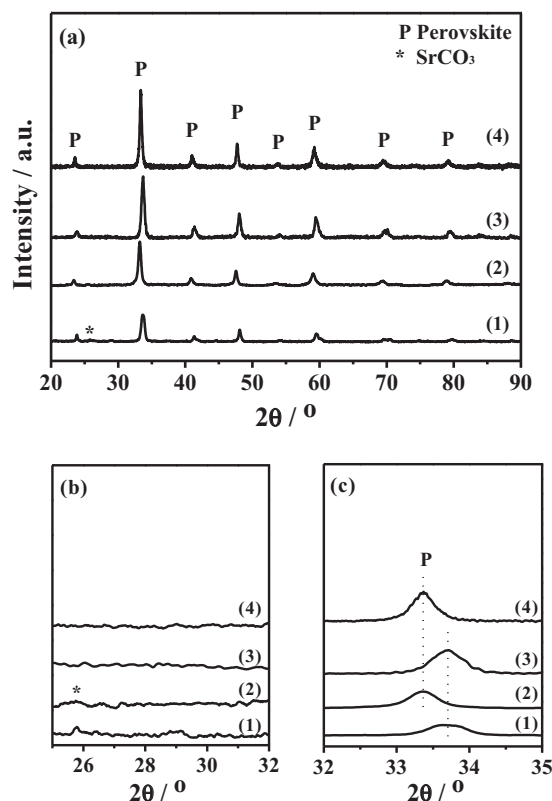


**Fig. 1.** (a) XRD patterns of the  $\text{La}_{0.7}\text{Sr}_{0.3}\text{Co}_{1-x}\text{Fe}_x\text{O}_3$  catalysts; (b) and (c) zoom-in of the pattern (a) at the different diffraction angle regions: (1) Fe-0-S; (2) Fe-2-S; (3) Fe-0-F; and (4) Fe-2-F.

air could inhibit the formation of the carbonate and/or highly disperse small carbonate crystallites on the catalysts. Probably, both factors would influence the catalytic activities.

Furthermore, the intensity of the perovskite diffraction peaks became stronger and sharper, and shifted toward small diffraction angles (Fig. 1(c)) after Fe-doping. It suggests the successfully partial substitution of the  $\text{Co}^{3+}$  cations ( $r_{\text{Co}^{3+}} = 0.0610\text{ nm}$ ) with the larger  $\text{Fe}^{3+}$  cations ( $r_{\text{Fe}^{3+}} = 0.0645\text{ nm}$ ) [37]. Thus, the Fe doping induced the expansion of the perovskite unit cell, as well as the improved crystallinity degree of the perovskite phases.

The average grain size (uncorrected) of the perovskite phase for each catalyst was calculated with the Scherrer equation using its strongest diffraction peak in Fig. 1(c), and the results were listed in Table 1. Apparently, the partial substitution of cobalt with iron cations enlarged the  $D$  values, and, especially, the calcination in flowing air was beneficial to the formation of the relatively more complete perovskite structure.

The BET surface areas of the catalysts are also gathered in Table 1. Compared with the Fe-0-S and the Fe-0-F catalysts, the calcination in flowing air could increase the catalyst's surface area. The precursor calcined in flowing air can remove intense heat caused by the combustion of the residual CA and EDTA, and, thus, avoid the sintering of the catalyst. It can also purge the produced  $\text{CO}_2$  therein

**Table 1**

The average particle size of the perovskite phase and the BET surface area of the catalysts.

Catalysts	Fe-0-S	Fe-2-S	Fe-0-F	Fe-2-F
$D$ (nm) <sup>a</sup>	13.3	14.1	15.4	20.5
BET ( $\text{m}^2/\text{g}$ )	16.6	14.2	19.8	13.9

<sup>a</sup>  $D$ : the average particle size calculated (uncorrected) by the Scherrer equation with the (1 2 1) facet.

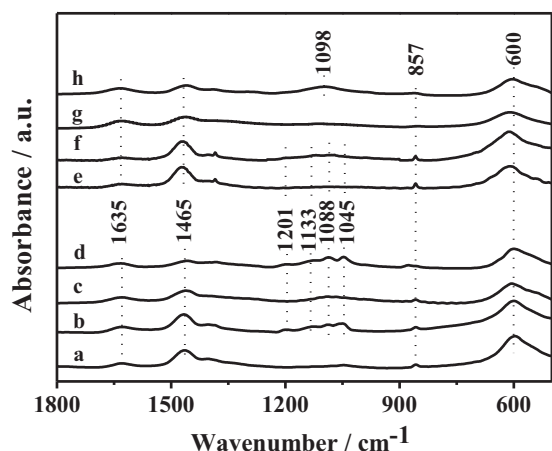


**Fig. 2.** FT-IR spectra of the  $\text{La}_{0.7}\text{Sr}_{0.3}\text{Co}_{1-x}\text{Fe}_x\text{O}_3$  catalysts: (a) the fresh Fe-0-S; (b) the sulfated Fe-0-S; (c) the fresh Fe-0-F; (d) the sulfated Fe-0-F; (e) the fresh Fe-2-S; (f) the sulfated Fe-2-S; (g) the fresh Fe-2-F; and (h) the sulfated Fe-2-F.

out of the furnace quickly, inhibiting the formation of carbonate, which has been evidenced by XRD in Fig. 1(b).

### 3.2. Characterizations of the fresh and pre-sulfated $\text{La}_{0.7}\text{Sr}_{0.3}\text{Co}_{1-x}\text{Fe}_x\text{O}_3$ catalysts

The FT-IR spectra of the catalysts before and after sulfation at 300 °C are distinctly shown in Fig. 2. The band at about 600  $\text{cm}^{-1}$  belongs to the characteristic vibration of perovskite [19,38]. The band at 1635  $\text{cm}^{-1}$  is assigned to the bending vibration of  $\text{H}_2\text{O}$  molecules adsorbed from atmosphere. Interestingly, the vibration bands at 857 and 1465  $\text{cm}^{-1}$ , which can be ascribed to the vibration of the carbonate species [33,39], are also observed, although no carbonate phase was detected from the XRD patterns of the Fe-0-F and Fe-2-F catalysts. It reveals the existence of the highly dispersed carbonate crystallites on the Fe-0-F and Fe-2-F catalysts, since the XRD technique can only identify the long-range-order materials. Compared with Fig. 2(a), (c) and (g), the FT-IR spectra of the fresh Fe-0-F and Fe-2-F catalysts show the weaker intensity of the vibration bands belonging to the carbonates species. It suggests that the calcination in flowing air can reduce the amount of the carbonates in the catalyst effectively, which is in a good agreement with the XRD results. Moreover, the intensity of the IR band belonging to carbonate of the Fe-0-F catalyst was slightly stronger as compared with the Fe-2-F catalyst. It indicates that the Fe-doping reduced the amount of the residual carbonate on the catalyst.

For the sulfated Fe-0-S, Fe-0-F and Fe-2-S catalysts (Fig. 2(b), (d) and (f)), four vibration bands appeared at 1201, 1133, 1088 and 1045  $\text{cm}^{-1}$ , which can be assigned to the sulfate species [40]. The bands at 1133, 1088 and 1045  $\text{cm}^{-1}$  belong to the S–O symmetric stretching vibrations of the alkaline-earth sulfates, while the band at 1201  $\text{cm}^{-1}$  may be attributed to some stable bulk sulfate species [17]. For the sulfated Fe-2-F catalyst (Fig. 2(h)), only one weakly broad band ranging from 1170 to 950  $\text{cm}^{-1}$  is visible and centered at 1098  $\text{cm}^{-1}$ , and no obvious bulk sulfate is detected. This broad band is hardly identified, and probably belongs to the superficial sulfate species. Therefore, it is expected that the Fe-2-F catalyst may possess an improved sulfur tolerance.

The SEM images of the fresh and sulfated catalysts are shown in Fig. 3 aiming to determine their micro-morphologies. The particle-size of the Fe-0-S catalyst as shown in Fig. 3(a) was widely distributed from 50 to 150 nm in various shapes. And the particles were prone to aggregation by forming irregular lumps, as a result of the serious sintering. Interestingly, the calcination in flowing air generated the relatively homogeneous particle-size distribution in

regular shapes (a diameter of about 80 nm) for both the Fe-0-F and Fe-2-F catalysts (Fig. 3(e) and (g)).

After the pre-sulfation treatment, the morphologies of these catalysts differently varied. The crush of the Fe-0-S, Fe-2-S and Fe-0-F particles into the small pieces by sulfation was clearly observed in Fig. 3(b), (d) and (f). Nevertheless, little change was observed for the Fe-2-F catalyst after sulfation as shown in Fig. 3(g) and (h). This may result in a stably mechanical strength and structural stability during its real application for automotive cars in future.

The  $\text{H}_2$ -TPR experiments of the  $\text{Co}_2\text{O}_3$ ,  $\text{Fe}_2\text{O}_3$ , Fe-0-F and Fe-2-F samples were conducted to elucidate their different sulfur tolerance behavior, and the results are shown in Fig. 4. Before the  $\text{H}_2$ -TPR tests, the standard  $\text{Co}_2\text{O}_3$  and  $\text{Fe}_2\text{O}_3$  samples were calcined at 800 °C for 2 h to provide more comparable information to the perovskite catalysts. In the  $\text{H}_2$ -TPR profile of the  $\text{Co}_2\text{O}_3$  sample (Fig. 4(a)), three reduction peaks were observed. The stronger reduction peaks centered at 359 and 463 °C were ascribed to the reduction of  $\text{Co}^{3+}$  to  $\text{Co}^{2+}$  and  $\text{Co}^{2+}$  to  $\text{Co}^0$  [41], respectively. And the weakest one centered at 776 °C was probably due to the reduction of the bulk cobalt oxides. For the reduction of the  $\text{Fe}_2\text{O}_3$  sample, the sharp reduction peak centered at 437 °C was attributed to the reduction of  $\text{Fe}_2\text{O}_3$  to  $\text{Fe}_3\text{O}_4$ , while the followed broad peak was assigned to the reduction of  $\text{Fe}_3\text{O}_4$  to FeO and FeO to  $\text{Fe}^0$  [28].

In Fig. 4(b), a weak  $\text{H}_2$  consumption peak located below 300 °C was observed for the Fe-0-F catalysts. As a result of the electrically neutral principles, some abnormal tetravalent cobalt cations may exist on the  $\text{La}_{0.7}\text{Sr}_{0.3}\text{CoO}_3$  perovskite. Therefore, this reduction peak might be ascribed to the reduction of the chemically absorbed oxygen [30], as well as  $\text{Co}^{4+}$  to  $\text{Co}^{3+}$ . For the fresh  $\text{La}_{0.7}\text{Sr}_{0.3}\text{CoO}_3$  catalyst the broad peak from 350 to 450 °C was assigned to the reduction of  $\text{Co}^{3+}$  to  $\text{Co}^{2+}$ , and the reduction peak ranged from 450 to 600 °C might be correlated to the reduction of  $\text{Co}^{2+}$  to  $\text{Co}^0$  [42]. The high-temperature reduction peak above 700 °C might be attributed to the reduction of the bulk cobalt oxides as discussed in Fig. 4(a). After the sulfation treatment, the position of the reduction peaks of  $\text{Co}^{3+}$  to  $\text{Co}^{2+}$  and  $\text{Co}^{2+}$  to  $\text{Co}^0$  shifted to higher temperatures. Additionally, the reduction peak centered at 564 °C of the sulfated Fe-0-F became broader and stronger than that of the fresh one. It indicates that this reduction peak might be overlapped by the reduction of both  $\text{Co}^{2+}$  and sulfate.

After the partial substitution of Co with Fe cations, the  $\text{H}_2$ -TPR profile of the fresh Fe-2-F catalyst, as shown in Fig. 4(c1), presented complex variations because of the presence of the residual cobalt and iron oxides besides the perovskites [43]. The reduction peak, owing to the reduction of the adsorbed gaseous oxygen, probably as well as  $\text{Fe}^{4+}$  to  $\text{Fe}^{3+}$  [44,45] and  $\text{Co}^{4+}$  to  $\text{Co}^{3+}$ , was observed at the similar temperature range as compared with the Fe-0-F catalyst. The broad reduction peak centered at 407 °C was due to the reduction of  $\text{Co}^{3+}$  to  $\text{Co}^{2+}$  and  $\text{Fe}^{3+}$  to  $\text{Fe}^{2+}$  in the perovskite [43], while the reduction peak from about 460 to 540 °C might be correlated to the reduction of the residual  $\text{Fe}_2\text{O}_3$  to  $\text{Fe}_3\text{O}_4$  [28]. Here, the iron species would induce a higher reduction temperature than the cobalt based catalyst [43,46], and the reduction peaks ranged from 600 to 840 °C might be due to the reduction of  $\text{Co}^{2+}$  and  $\text{Fe}^{2+}$  cations in perovskites to metals. Herein, the reduction peaks of the bulk perovskite and/or other metal oxides had the similar reduction temperature as indicated in Fig. 4(a). Thus, the reduction of  $\text{Fe}_3\text{O}_4$  to  $\text{Fe}^{2+}$  and  $\text{Fe}^{2+}$  to  $\text{Fe}^0$  for the residual  $\text{Fe}_2\text{O}_3$  might also occur at this temperature [28,46–48].

Compared with the  $\text{H}_2$ -TPR profiles of the fresh and sulfated Fe-2-F catalysts (Fig. 4(c1) and (c2)), the similar reduction peaks were observed originating from the absorbed gaseous oxygen and the abnormal tetravalent cations at low temperatures. For the sulfated Fe-2-F catalyst, the reduction peak centered at 407 °C due to the trivalent cations became slightly thinner; meanwhile, the area of the reduction peak centered at 663 °C also dropped. This indicates



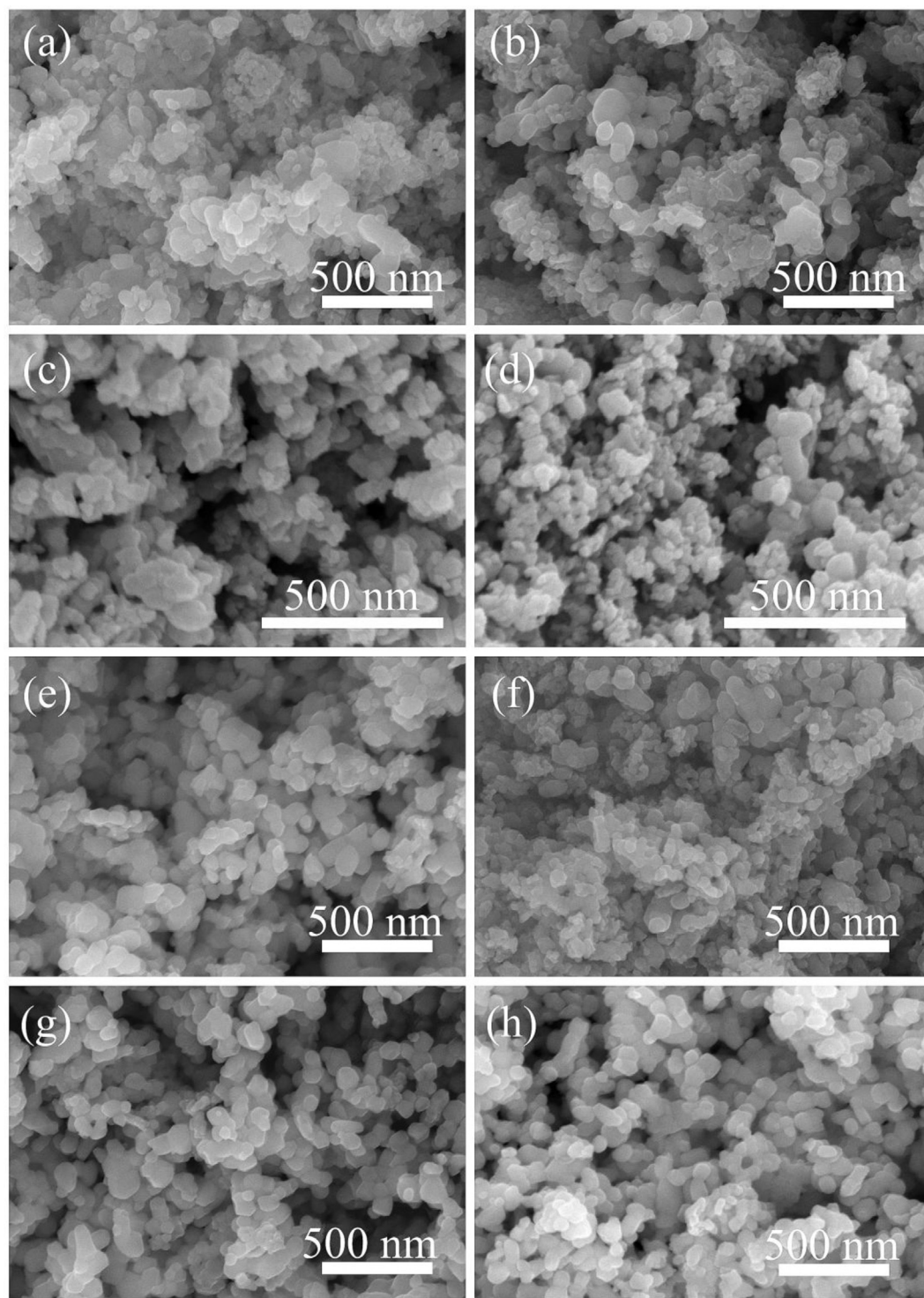


**Fig. 3.** SEM images of the  $\text{La}_{0.7}\text{Sr}_{0.3}\text{Co}_{1-x}\text{Fe}_x\text{O}_3$  catalysts: (a) the fresh Fe-0-S; (b) the sulfated Fe-0-S; (c) the fresh Fe-2-S; (d) the sulfated Fe-2-S; (e) the fresh Fe-0-F; (f) the sulfated Fe-0-F; (g) the fresh Fe-2-F; and (h) the sulfated Fe-2-F.

that the part of the cations in the perovskite may react with  $\text{SO}_2$  to form sulfates. Moreover, a new reduction peak centered at  $560^\circ\text{C}$ , the similar position with the sulfated Fe-0-F catalyst, simultaneously appeared in Fig. 4(c2). It might be contributed to the reduction of the deposited sulfates on the Fe-2-F catalyst. To confirm this assumption, the second  $\text{H}_2$ -TPR experiment was conducted as presented in Fig. 4(c3) after the sulfated catalyst underwent a general  $\text{H}_2$ -TPR test from room temperature to  $900^\circ\text{C}$ . The detailed experimental steps were described as follows: the catalyst after the first

$\text{H}_2$ -TPR run was cooled down to room temperature in the carrier gas ( $5\% \text{H}_2/\text{N}_2$ ), and then the second  $\text{H}_2$ -TPR experiment was conducted with the same conditions as the previous one. The obtained profile was almost a straight line (Fig. 4(c3)), which demonstrates the totally reduction of these (composite) metal oxides after the first  $\text{H}_2$ -TPR run. Thereafter, another  $\text{H}_2$ -TPR run (Fig. 4(c4)) was carried out after the catalyst was further treated by a pure oxygen flow at  $700^\circ\text{C}$  for 1 h and then cooled down to room temperature in the oxygen flow. Very interestingly, the profile presented in Fig. 4(c4)

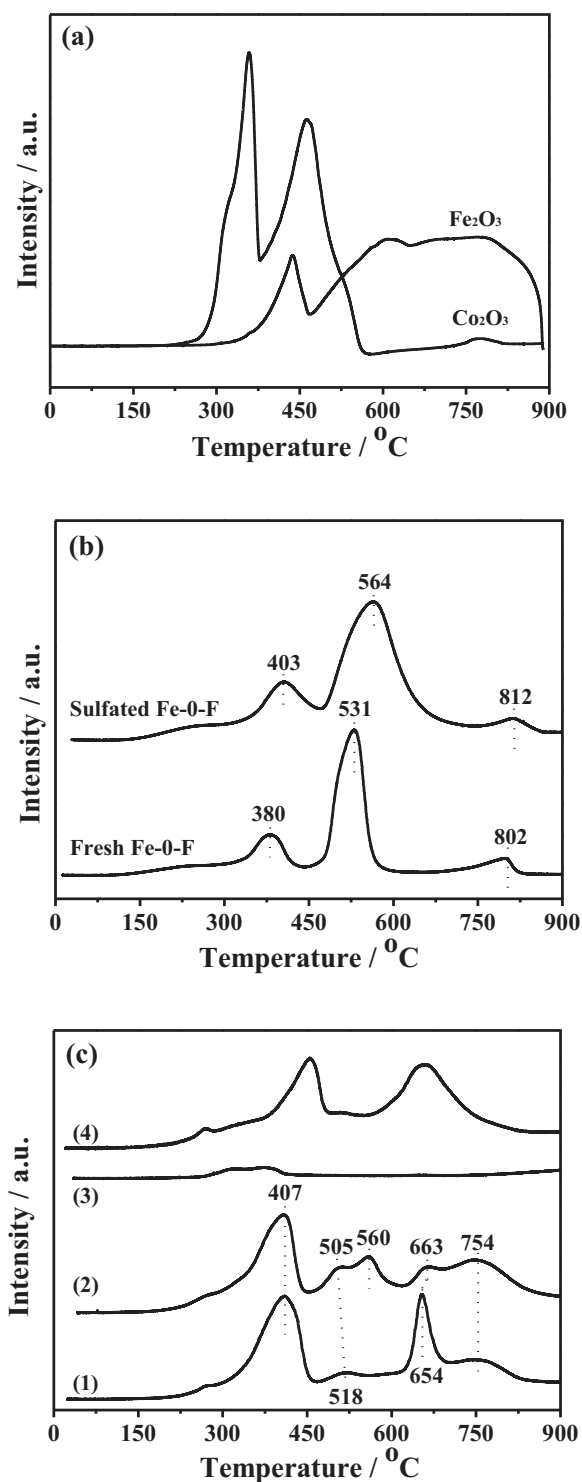


**Fig. 4.** H<sub>2</sub>-TPR profiles of (a) the standard Co<sub>2</sub>O<sub>3</sub> and Fe<sub>2</sub>O<sub>3</sub> samples; (b) the fresh and sulfated Fe-0-F catalysts; (c) the Fe-2-F catalyst: (1) the fresh catalyst; (2) the sulfated catalyst; (3) the repeated H<sub>2</sub>-TPR test just followed the first H<sub>2</sub>-TPR run of the catalyst (2); and (4) the repeated H<sub>2</sub>-TPR test followed the first H<sub>2</sub>-TPR run of the catalyst (2) which was further treated in the pure oxygen gas at 700 °C for 1 h.

was quite similar to the fresh one (Fig. 4(c1)), except that the reduction peak at 560 °C for the sulfated catalyst (Fig. 4(c2)) disappeared. These results strongly suggest that the peak centered at 560 °C was due to the reduction of the deposited sulfates on the catalysts.

To certify our assumption, H<sub>2</sub>-TPR-MS experiments for the fresh and sulfated Fe-2-F samples were also conducted and presented in

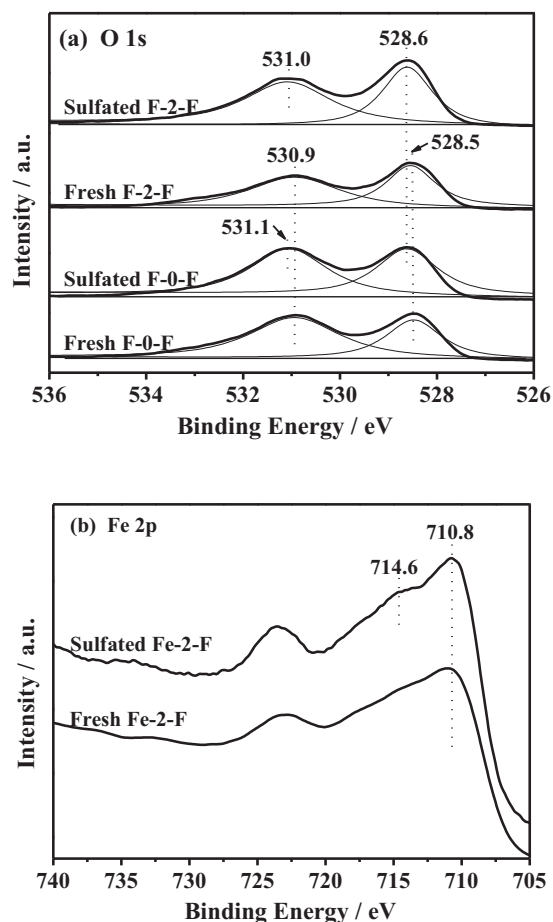


**Fig. 5.** XPS spectra of the La<sub>0.7</sub>Sr<sub>0.3</sub>Co<sub>1-x</sub>Fe<sub>x</sub>O<sub>3</sub> catalysts in the regions of (a) O 1s and (b) Fe 2p.

Fig. S2. Herein, the H<sub>2</sub>O and CO<sub>2</sub> trap was removed from the H<sub>2</sub>-TPR instrument as described in the experimental section, and a mass spectrometer was connected to the outlet gas replacing the TCD. As observed from the H<sub>2</sub>O profile (Fig. S2(a)), the shape and reduction temperature of the peaks for both the fresh and presulfated (for 1 h) samples was quite similar to those presented in Fig. 4c: after sulfation, a new reduction peak centered at 560 °C appeared. After the severe sulfation treatment (for 24 h), this peak was extremely strengthened. It strongly suggests that this reduction peak was resulted from the reduction of sulfates. Interestingly, no H<sub>2</sub>S peak was observed for the presulfated samples (Fig. S2(b)). Our previous study showed that the reduction of the presulfated Fe/BaO/Al<sub>2</sub>O<sub>3</sub> would produce BaS; H<sub>2</sub>S was produced only in the presence of Pt [49]. Therefore, in this work the sulfates might be reduced to metal sulfides, because of lacking noble metal. Moreover, from the SO<sub>2</sub> profile (Fig. S2(c)), no obvious SO<sub>2</sub> peak was detected for the sample presulfated for 1 h, but a broad desorption peak ranging from 400 to 620 °C was observed for the severely sulfated sample. It suggests that SO<sub>2</sub> might be the other reduction product from sulfates. From the CO<sub>2</sub> profile (Fig. S2(d)), we can clearly observe two desorption peaks at low and high temperatures, suggesting the presence of two kinds of carbonates [50]. However, we could not observe this desorption in Fig. 4, because the released CO<sub>2</sub> would be captured by the H<sub>2</sub>O and CO<sub>2</sub> trap equipped before the TCD.

The XPS experiments were employed to investigate the surface composition of the catalysts before and after the sulfation treatment. The XPS spectra in the O 1s region are shown in Fig. 5(a). Clearly, all of these spectra can be separated into two peaks. The low BE peak can be assigned to the surface lattice oxygen species

[48,51], whereas the high BE peak is originated from the adsorbed oxygen species [51,52], as well as a small amount of the residual carbonates. Herein, we approximately assume that the high BE peak was totally attributed to the adsorbed oxygen. After sulfation, the position of the BE peaks slightly shifted toward higher BE than that of the fresh one. This shift might be attributed to the formation of the sulfates ranging from 531.5 to 532.5 eV [53]. It can be inferred that more sulfates were deposited on the sulfated Fe-0-F catalyst than that on the sulfated Fe-2-F catalyst. It is in a good agreement with the catalytic test results that the Fe-2-F catalyst possesses the better sulfur resistance.

The XPS spectra in the O 1s region were further fitted by a standard Gaussian–Lorentzian deconvolution method in order to qualitatively compare the relative content of the different oxygen species corresponding to the low and high BE peaks. As listed in Table 2, the partial substitution of Co with Fe cations led to a drop of the  $O_{\text{HIGH}}/O_{\text{LOW}}$  value, indicating the decreased surface oxygen species, which may be involved in the  $\text{NO}_x$  storage reactions. After sulfation, the  $O_{\text{HIGH}}/O_{\text{LOW}}$  value dropped for both catalysts, probably because of the transformation of carbonates to sulfate, as well as the sulfur poison of the perovskite. Here, more oxygen species belonging to the high BE peak was lost from the Fe-0-F catalyst than that from the Fe-2-F catalyst. It indicates that the Fe-2-F catalyst possessed the higher sulfur tolerance.

The XPS spectra in the region of Fe 2p are also presented in Fig. 5(b). Two main BE peaks were observed, which belonged to Fe 2p<sub>1/2</sub> (BE >720 eV) and Fe 2p<sub>3/2</sub> (BE <720 eV). The BE peak centered at 710.8 eV in the Fe 2p<sub>3/2</sub> region indicates that the Fe element existed in the oxide form [54]. The broad BE peak centered at about 714.6 eV for the sulfated Fe-2-F catalysts was ascribed to the Fe<sup>3+</sup> cation in Fe<sub>2</sub>(SO<sub>4</sub>)<sub>3</sub> [28]. Therefore, the broad IR band centered at 1098 cm<sup>-1</sup> of the sulfated Fe-2-F catalyst in Fig. 2 (h) might be mainly contributed by Fe<sub>2</sub>(SO<sub>4</sub>)<sub>3</sub>. The Fe-doping in the perovskite crystal lattice could protect the NO<sub>x</sub> storage component, such as barium in BaFeO<sub>3-x</sub>, from sulfation [28]. Here, the Fe element was well dispersed surrounding the Sr element in perovskites, probably as well as the highly dispersed tiny carbonate crystallites. This would effectively protect both the strontium element in perovskites and the highly dispersed carbonates from the sulfur poisoning, and consequently maintain the NSC of the sulfated Fe-2-F catalysts compared with the fresh one. Herein, no obvious lanthanum sulfate species was observed for the pre-sulfated samples as displayed in Fig. S3.

The surface elemental composition of the catalysts determined from the XPS measurements is also listed in Table 2. Compared with their atomic ratio at the A site, the Fe-doping induced a higher La/Sr value. It could be inferred that there was less amount of the strontium element, which is the most important storage component in the catalyst, on the surface of the Fe-2-F catalyst. Accordingly, it is reasonable to expect a smaller NO<sub>x</sub> storage capacity of the Fe-2-F catalyst than that of the Fe-0-F catalyst. After sulfation, the La/Sr ratio slightly increased for both catalysts, indicating the drop of their NSC.

To obtain the local coordination structure information of the strontium and iron elements in the perovskites, the EXAFS measurements were performed. Fig. 6 shows the radial structural functions (RSFs) of the Sr K-edge of the Fe-0-F, Fe-2-F and standard SrSO<sub>4</sub> samples. The coordination peak at around 0.195 nm was assigned to the first Sr–O shell, and the one at around 0.271 nm was contributed by the first Sr–Sr and Sr–La shells for the scattering paths of the Fe-2-F and Fe-0-F catalysts [55]. Here, the magnitude of the first Sr–O coordination peak of the Fe-0-F catalyst, correlating to the coordination number, suffers a dramatic change after sulfation, and is very close to the standard SrSO<sub>4</sub> sample. It indicates that the storage sites, i.e. the strontium oxides, were poisoned after the sulfation treatment by forming SrSO<sub>4</sub>. However, the coordination

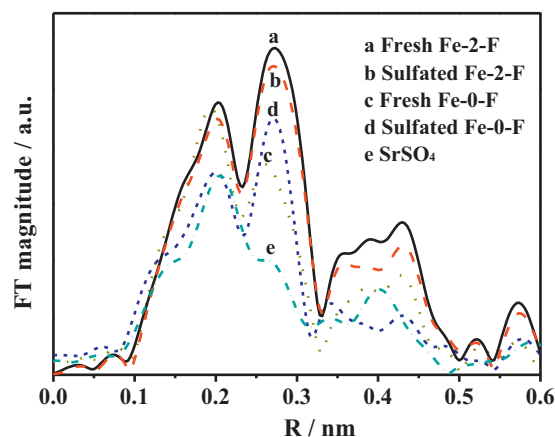


Fig. 6. RSFs of the Sr K-edge.

peak of the first Sr–O shell including the magnitude and the shape had little change for the sulfated Fe-2-F catalyst compared with the fresh Fe-2-F catalyst.

The RSFs of the Fe K-edge of the fresh and sulfated Fe-2-F catalyst, as well as the standard Fe<sub>2</sub>(SO<sub>4</sub>)<sub>3</sub> sample, are shown in Fig. 7 to further illuminate the local coordination structures of Fe in the sulfated Fe-2-F catalyst. The first coordination peak of the fresh Fe-2-F catalyst at 0.132 nm was contributed to the first Fe–O shell in perovskite. After sulfation, the intensity of the peak increased, and the position of the peak shifted to 0.141 nm, which is the similar coordination distance with the first Fe–O shell in the standard Fe<sub>2</sub>(SO<sub>4</sub>)<sub>3</sub> sample, revealing the formation of the Fe<sub>2</sub>(SO<sub>4</sub>)<sub>3</sub> species on the sulfated Fe-2-F catalyst. Combining with the EXAFS results of the Sr K-edge and Fe K-edge, we can conclude that the Fe dopants in the La<sub>0.7</sub>Sr<sub>0.3</sub>Co<sub>0.8</sub>Fe<sub>0.2</sub>O<sub>3</sub> perovskite prevent the strontium element from sulfation. This is in a good agreement with the FT-IR and XPS results. To the best of our knowledge, it is for the first time to certify that during the sulfation process the sulfur is preferential to react with the iron in perovskite from the viewpoint of the local atomic coordination. In addition, this is also a very crucial discovery not only for the effect of iron in perovskite on sulfur tolerance but also for the desulfation process. The H<sub>2</sub>-TPR profiles of the standard Fe<sub>2</sub>(SO<sub>4</sub>)<sub>3</sub> and SrSO<sub>4</sub> (Fig. S4) apparently showed that the bulk Fe<sub>2</sub>(SO<sub>4</sub>)<sub>3</sub> can be reduced at the much lower temperature than the bulk SrSO<sub>4</sub>. It indicates that De-sulfur will occur at a lower temperature for the Fe-2-F catalyst.

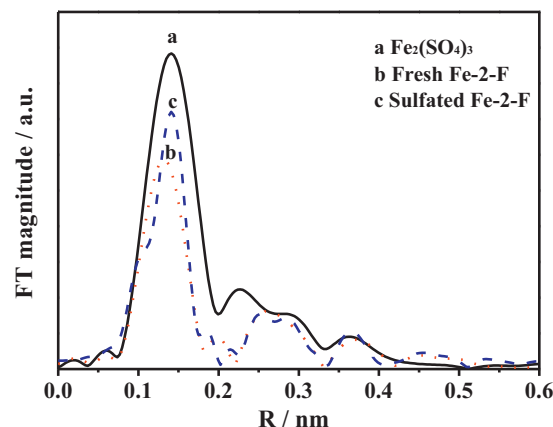


Fig. 7. RSFs of the Fe K-edge.



**Table 2**

The surface elemental analysis of the catalysts determined by XPS.

Catalysts	Surface elemental composition (%)						Relative proportion (%)	
	La	Sr	Co	Fe	O	S	La/Sr	O <sub>HIGH</sub> /O <sub>LOW</sub>
Fresh Fe-0-F	15.0	5.9	12.5	–	66.6	–	2.54	2.13
Sulfated Fe-0-F	15.6	6.0	12.3	–	65.6	0.5	2.62	1.70
Fresh Fe-2-F	16.2	5.5	10.4	2.5	65.4	–	2.95	1.50
Sulfated Fe-2-F	17.1	5.8	10.9	2.4	63.0	0.7	2.97	1.38

### 3.3. Catalytic tests

The NSC and NO-to-NO<sub>2</sub> conversion of the catalysts before and after the SO<sub>2</sub>/O<sub>2</sub> treatment are listed in Table 3. Obviously, these perovskites had an excellent NO oxidation ability, and presented a high NO-to-NO<sub>2</sub> conversion. It is very interesting that the NO-to-NO<sub>2</sub> conversion has little difference for each pair of the fresh and sulfated catalysts. It indicates that the sulfation has little effect on the NO oxidation ability.

The catalysts calcined in static air had much larger NSC values than those calcined in flowing air. For example, the NSC of the Fe-0-S and Fe-2-S catalysts was 776.7 and 739.7 μmol/g, respectively, whereas the NSC of the Fe-0-F and Fe-2-F catalysts drastically dropped to 487.1 and 385.4 μmol/g, respectively. The XRD (Fig. 1) and FT-IR (Fig. 2) results indicate that the Fe-doping and the flowing atmosphere (air) during the calcination improved the crystallinity degree of the perovskites and reduced the amount of the carbonates, especially for the bulk ones. The NO<sub>x</sub> storage results herein coincide with our previous studies [28–30] that the presence of the carbonate phase in the perovskite catalysts could synergistically enhance its NSC. Additionally, the NSC values also dropped with the Fe-doping. The decrease of the NSC is probably resulted from the reduced amount of the carbonates remained on the catalysts.

The NO<sub>x</sub> storage profiles of the Fe-0-S, Fe-2-S, Fe-0-F and Fe-2-F catalysts are plotted in Fig. 8 to determine the variation of the NO and NO<sub>2</sub> concentration. Clearly, NO<sub>x</sub> could be totally trapped with the different durations for each catalyst. As observed from the NO<sub>x</sub> storage profile of the fresh Fe-0-S catalyst (Fig. 8(a)), NO could be totally trapped for 10.8 min. It is very interesting that the fully trapping period for NO<sub>2</sub> is about 1.5 min longer than that for NO. Thereafter, the NO<sub>2</sub> concentration gradually increased, and ultimately became constant. However, the variation of the NO concentration presented a different behavior that the concentration firstly increased and then gradually decreased. After a prolonged period, it became stable associated with the NO<sub>2</sub> concentration. The fresh Fe-2-S catalyst presented the similar NO<sub>x</sub> storage behavior with the fresh Fe-0-S catalyst as shown in Fig. 8(c).

NO<sub>2</sub> could directly and effectively react with the basic NO<sub>x</sub> storage components, e.g. basic metal oxide and carbonate, through a disproportionation reaction to produce nitrate and release NO. However, NO is hardly stored on the NO<sub>x</sub> storage components from the NO/O<sub>2</sub> feeding without the aid of noble metals [56,57], because little NO<sub>2</sub> would be produced therein.

As for the perovskite-type catalysts herein, we carried out the NO adsorption and NO<sub>2</sub> adsorption experiments, respectively, in

the absence of O<sub>2</sub>, as shown in Fig. S5. For the NO adsorption alone (Fig. S5(a)), the NO<sub>2</sub> signal sharply increased at the initial period, and then quickly dropped. This NO<sub>2</sub> pulse might be resulted from the NO oxidation with the chemically adsorbed oxygen on the perovskite: when the actively oxygen species was thoroughly consumed, the NO<sub>2</sub> signal immediately dropped to its initial level, i.e. nearly zero. Thereafter, the NO signal gradually decreased and reached the minimum concentration about 520 ppm, and then increased to its initial concentration. It indicates that NO alone was difficultly stored on the catalyst. Regarding the NO<sub>2</sub> adsorption alone (Fig. S5(b)), a NO<sub>x</sub> trap could be well formed, demonstrating the high efficiency of NO<sub>2</sub> in the NO<sub>x</sub> storage. When the NO<sub>x</sub> storage process reached the equilibrium, the NO<sub>2</sub> content is about 83.0%, the similar value to the results of the NO/O<sub>2</sub> coadsorption in Table 3. Moreover, we compared the FT-IR spectra of the Fe-2-F sample under the different treatments (Fig. S6). Clearly, little nitrate was formed on the sample after adsorbing NO alone; the FT-IR spectra for the sample adsorbing NO<sub>2</sub> alone and NO/O<sub>2</sub> coadsorption had little difference that a lot of nitrates were formed. These findings coincide with the NO<sub>x</sub> storage results presented in Fig. S1 and S5.

According to the above mentioned results, the NO<sub>x</sub> storage steps for the fresh Fe-0-S and Fe-2-S catalysts might be described as follows:

- NO might adsorb on the perovskite or directly form nitrates with the aid of oxygen.
- The adsorbed NO reacted with the chemisorbed oxygen on the perovskite to form NO<sub>2</sub>.
- The generated NO<sub>2</sub> herein was readily trapped in the form of nitrates on the catalyst.
- The NO adsorption sites on the perovskite were fully occupied; meanwhile the NO adsorption and oxidation to produce and release NO<sub>2</sub> on the perovskite might reach equilibrium.
- The NO produced from the NO<sub>2</sub> disproportionation would release out of the reactor due to the saturated NO adsorption on the perovskites, and appeared in the outlet gas.
- Although the total NO<sub>x</sub> storage process finished over the perovskite phase, NO<sub>2</sub> could still be trapped by the excessive carbonates continuously.

These reaction routes explain why the trapping period for NO<sub>2</sub> is slightly longer than that for NO as observed in Fig. 8(a) and (c).

As shown in Fig. 8(e) and (g), the NO<sub>x</sub> fully trapping period of the Fe-0-F and Fe-2-F catalysts became shorter (about 4.5–5.5 min), and the difference for the duration of the NO and NO<sub>2</sub> traps was negligible. Combining with the NO<sub>x</sub> storage results of the Fe-0-S and Fe-2-S catalysts, it indicates that the residual carbonates therein play a significant role for enhancing the NO<sub>x</sub> storage capacity, and have more NO<sub>x</sub> storage sites than the perovskite phases. After we zoomed in the bottom of the NO<sub>x</sub> trapping curves, a tiny NO<sub>2</sub> signal (about 4 ppm) was detected for the Fe-2-F catalyst, but the NO signal kept constant at zero (Fig. 8(g)). It could be inferred that NO was fully oxidized to NO<sub>2</sub> or nitrates on the catalysts during forming the trap, but the insufficient carbonates on these catalysts led to slight escape of NO<sub>2</sub>. In contrast, at the bottom of

**Table 3**The NSC and NO-to-NO<sub>2</sub> conversion of the catalysts before and after sulfation.

Catalysts	NSC of the catalysts (μmol/g)		NO-to-NO <sub>2</sub> conversion (%)	
	Fresh	Sulfated	Fresh	Sulfated
Fe-0-S	776.7	326.5	83.0	82.9
Fe-2-S	739.7	473.0	84.6	85.6
Fe-0-F	487.1	274.8	84.0	83.3
Fe-2-F	385.4	360.7	85.3	84.7



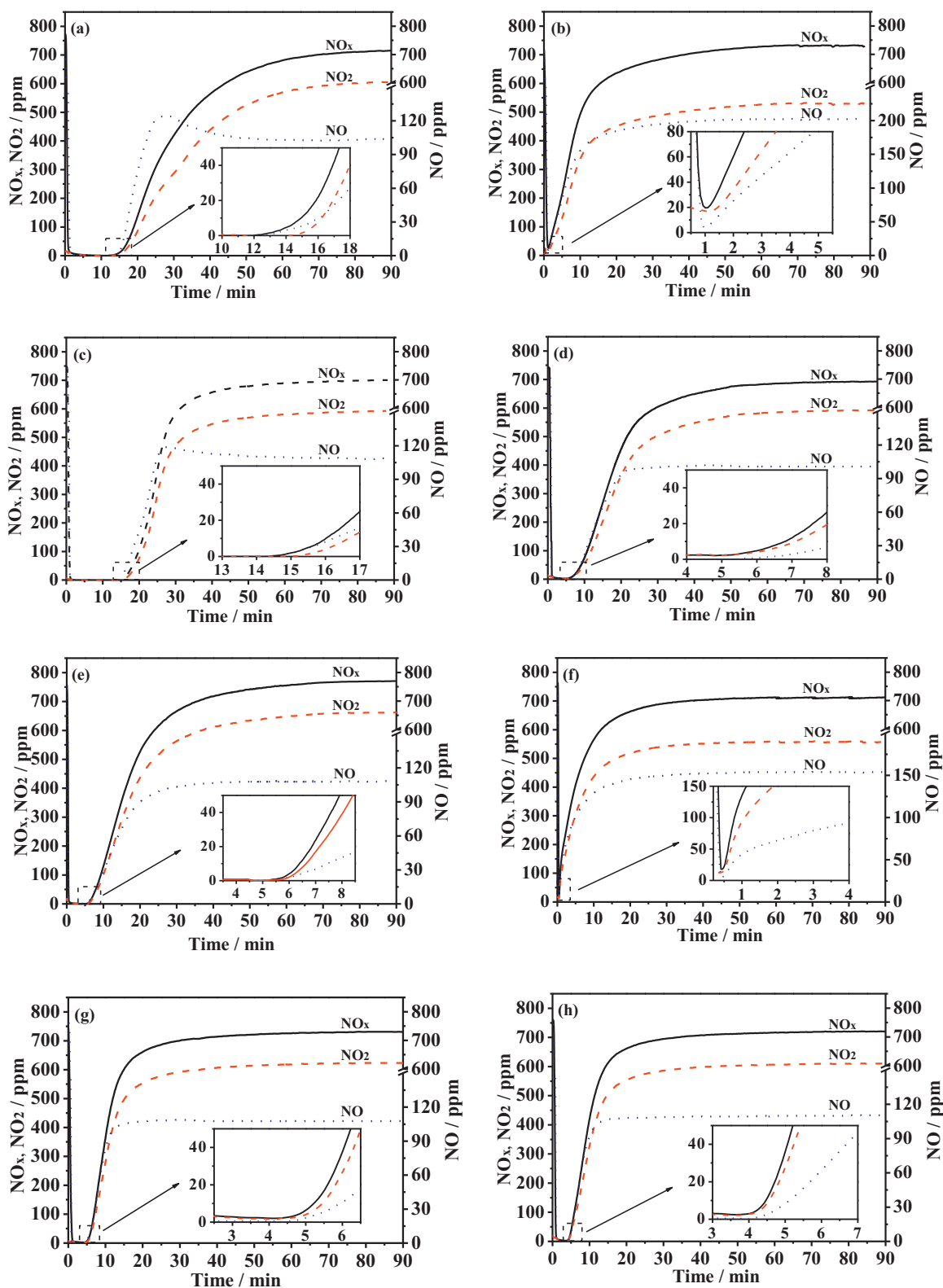


**Fig. 8.** NO<sub>x</sub> storage profiles of the La<sub>0.7</sub>Sr<sub>0.3</sub>Co<sub>1-x</sub>Fe<sub>x</sub>O<sub>3</sub> catalysts: (a) the fresh Fe-0-S; (b) the sulfated Fe-0-S; (c) the fresh Fe-2-S; (d) the sulfated Fe-2-S; (e) the fresh Fe-0-F; (f) the sulfated Fe-0-F; (g) the fresh Fe-2-F; and (h) the sulfated Fe-2-F.

the trap, both the NO and NO<sub>2</sub> signals of the Fe-0-F catalyst were zero, indicating more carbonates in the Fe-0-F catalyst than that in the Fe-2-F. This has been confirmed by the FT-IR results in Fig. 2. The schematic drawing of the NO<sub>x</sub> storage process is shown in Fig. 9.

After the SO<sub>2</sub>/O<sub>2</sub> pretreatment, the NSC for all catalysts decreased in different degrees. Among these catalysts, the Fe-0-S catalyst had the most severe drop (Table 3 and Fig. 8(b)). The lowest NO<sub>x</sub> concentration was around 20 ppm, and could not form a NO<sub>x</sub> trap efficiently. Moreover, the NO<sub>2</sub> concentration is always

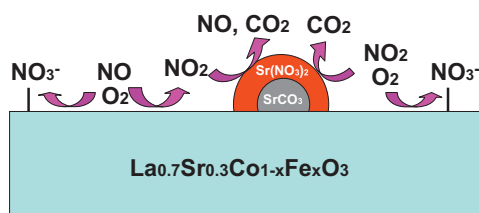


**Fig. 9.** The schematic drawing of the  $\text{NO}_x$  storage process on the  $\text{La}_{0.7}\text{Sr}_{0.3}\text{Co}_{1-x}\text{Fe}_x\text{O}_3$  catalyst.

higher than NO at the bottom of the trap. The similar tendency was observed for the Fe-0-F catalyst as shown in Fig. 8(f). It reveals that the Fe-0-S and Fe-0-F catalysts, which do not contain iron, were seriously poisoned by  $\text{SO}_2$ , regardless of the amount of carbonates existing in the catalysts. After the Fe-doping, a thorough  $\text{NO}_x$  trap could be formed for the Fe-2-S and Fe-2-F catalysts, but the length of the trap became shorter, especially for the Fe-2-S catalyst. Little difference was observed from the  $\text{NO}_x$  storage profiles of the fresh and sulfated Fe-2-F catalysts as shown in Fig. 8(g) and (h). The decreasing NSC of the Fe-2-S catalyst might be mainly due to the sulfation of the bulk carbonates in it. It indicates that the addition of iron into the perovskite-type catalysts could improve their sulfur tolerance. However, the large quantity of the bulk carbonates in the Fe-2-S catalyst was more easily poisoned by sulfur as compared with the Fe-2-F catalyst. The strontium in the Fe-2-F catalyst was hardly sulfated by preferentially forming  $\text{Fe}_2(\text{SO}_4)_3$  to maintain its NSC after pre-sulfated treatment, as indicated by the FT-IR, EXAFS and XPS results.

Among the catalysts reported in this work and before (Table S1), the NSC of the Fe-2-F catalyst only dropped 6.4% after sulfation; while the NO-to- $\text{NO}_2$  conversion kept constant at around 85% before and after sulfation. Undoubtedly, the Fe-2-F catalyst presented the best sulfur-resistance performance.

#### 4. Conclusion

The  $\text{La}_{0.7}\text{Sr}_{0.3}\text{Co}_{1-x}\text{Fe}_x\text{O}_3$  ( $x=0, 0.2$ ) perovskite catalysts were prepared by a complexation method. Their  $\text{NO}_x$  storage capacity, ability of NO oxidized to  $\text{NO}_2$  and sulfur tolerance were investigated in detail. All of the  $\text{La}_{0.7}\text{Sr}_{0.3}\text{Co}_{1-x}\text{Fe}_x\text{O}_3$  catalysts have a high NO-to- $\text{NO}_2$  oxidation ability and a large NSC. The formed  $\text{NO}_2$  would be efficiently trapped over the residual carbonates and the perovskites by forming nitrates. The bulk carbonates could enhance the NSC, but was readily poisoned by sulfur.

The treatment by calcination in flowing air during the catalyst preparation can take away most of  $\text{CO}_2$  produced by citric acid and EDTA combustion promptly. Thus, the carbonates formation, especially for the bulk carbonates, was effectively inhibited and the residual carbonates were highly dispersed on the catalysts. Moreover, the addition of Fe could improve the perovskite crystallinity and probably reduce the amount of the carbonates. All of these factors improved the sulfur tolerance of the perovskite-type  $\text{La}_{0.7}\text{Sr}_{0.3}\text{Co}_{0.8}\text{Fe}_{0.2}\text{O}_3$  catalyst. Nevertheless, it also brings the drop of the NSC. Among these perovskite catalysts, the Fe-2-F catalyst in the  $\text{La}_{0.7}\text{Sr}_{0.3}\text{Co}_{0.8}\text{Fe}_{0.2}\text{O}_3$  formula exhibited the best sulfur tolerance: the NSC only dropped 6.4% after the sulfation treatment, and the NO-to- $\text{NO}_2$  conversion kept constant at around 85% before and after sulfation.

#### Acknowledgements

This work was financially supported by the National Natural Science Foundation of China (U1162103, U1232118), the “863 Program” of the Ministry of Science & Technology of China

(2008AA06Z323), the Natural Science Foundation of Tianjin (11JCY-BJC03700), the Program for New Century Excellent Talents in University of China (NCET-10-0615), the Program for Introducing Talents of Discipline to Universities of China (No. B06006), the State Key Laboratory of Coal Conversion (No. J12-13-902) and the Key Laboratory for Green Chemical Technology of Ministry of Education, Tianjin University.

#### Appendix A. Supplementary data

Supplementary data associated with this article can be found, in the online version, at <http://dx.doi.org/10.1016/j.apcatb.2013.06.005>.

#### References

- [1] J.E. Parks II, *Science* 327 (2010) 1584.
- [2] J. Wang, Y.Y. Ji, Z.W. He, M. Crocker, M. Dearth, R.W. McCabe, *Applied Catalysis B* 111 (2012) 562.
- [3] B. Pereda-Ayo, D. Duraiswami, J.A. González-Marcos, J.R. González-Velasco, *Chemical Engineering Journal* 169 (2011) 58.
- [4] N. Takahashi, H. Shinjoh, T. Iijima, T. Suzuki, K. Yamazaki, K. Yokota, H. Suzuki, N. Miyoshi, S. Matsumoto, T. Tanizawa, T. Tanaka, S. Tateishi, K. Kasahara, *Catalysis Today* 27 (1996) 63.
- [5] L. Lietti, P. Forzatti, I. Nova, E. Tronconi, *Journal of Catalysis* 204 (2001) 175.
- [6] B. Pereda-Ayo, J.R. González-Velasco, R. Burch, C. Hardacre, S. Chansai, *Journal of Catalysis* 285 (2012) 177.
- [7] E. Tronconi, I. Nova, C. Ciardelli, D. Chatterjee, G. Bandl-Konrad, T. Burkhardt, *Catalysis Today* 105 (2005) 529.
- [8] P. Granger, V.I. Parvulescu, *Chemical Reviews* 111 (2011) 3155.
- [9] S. Roy, A. Baiker, *Chemical Reviews* 109 (2009) 4054.
- [10] X. Li, M. Meng, P. Lin, Y. Fu, T. Hu, Y. Xie, J. Zhang, *Chemical Engineering Research and Design* 80 (2002) 190.
- [11] X. Li, M. Meng, P. Lin, Y. Fu, T. Hu, Y. Xie, J. Zhang, *Topics in Catalysis* 22 (2003) 111.
- [12] W. Epling, L. Campbell, A. Yezerets, N. Currier, J. Parks, *Catalysis Reviews: Science and Engineering* 46 (2004) 163.
- [13] T.J. Toops, D.B. Smith, W.S. Epling, J.E. Parks, W.P. Partridge, *Applied Catalysis B* 58 (2005) 255.
- [14] F.E. López-Suárez, M.J. Illán-Gómez, A. Bueno-López, J.A. Anderson, *Applied Catalysis B* 104 (2011) 261.
- [15] E. Fridell, H. Persson, L. Olsson, B. Westerberg, A. Amberntsson, M. Skoglundh, *Topics in Catalysis* 16/17 (2001) 133.
- [16] J.P. Breen, M. Marella, C. Pistarino, J. Ross, *Catalysis Letters* 80 (2002) 123.
- [17] C. Sedlmair, K. Seshan, A. Jentys, J. Lercher, *Catalysis Today* 75 (2002) 413.
- [18] H. Mahzoul, L. Limousy, J.F. Brilhac, P. Gilot, *Journal of Analytical and Applied Physics* 56 (2000) 179.
- [19] J. Liu, Z. Zhao, C. Xu, A. Duan, G. Jiang, *Journal of Physical Chemistry C* 112 (2008) 5930.
- [20] C. Kim, G. Qi, K. Dahlberg, W. Li, *Science* 327 (2010) 1624.
- [21] X. He, M. Meng, J. He, Z. Zou, X. Li, Z. Li, Z. Jiang, *Catalysis Communications* 12 (2010) 165.
- [22] I. Rosso, E. Garrone, F. Geobaldo, B. Onida, G. Saracco, V. Specchia, *Applied Catalysis B* 30 (2001) 61.
- [23] H. Wang, Y.F. Zhu, R.Q. Tan, W.Q. Yao, *Catalysis Letters* 82 (2002) 199.
- [24] S. Hodjati, C. Petit, V. Pitchon, A. Kiennemann, *Applied Catalysis B* 30 (2001) 247.
- [25] K. Yamazaki, T. Suzuki, N. Takahashi, *Applied Catalysis B* 30 (2001) 459.
- [26] P.T. Fanson, M.R. Horton, W.N. Delgass, J. Lauterbach, *Applied Catalysis B* 46 (2003) 393.
- [27] X. Li, J. Chen, P. Lin, M. Meng, Y. Fu, J. Tu, Q. Li, *Catalysis Communications* 5 (2004) 25.
- [28] H. Xian, X. Zhang, X. Li, L. Li, H. Zou, M. Meng, Q. Li, Y. Tan, N. Tsubaki, *Journal of Physical Chemistry C* 114 (2010) 11844.
- [29] H. Xian, X. Zhang, X. Li, H. Zou, M. Meng, Z. Zou, L. Guo, N. Tsubaki, *Catalysis Today* 158 (2010) 215.
- [30] H. Xian, F. Li, X. Li, X. Zhang, M. Meng, T. Zhang, N. Tsubaki, *Fuel Processing Technology* 92 (2011) 1718.
- [31] F. Li, L. Guo, H. Xian, M. Meng, Z. Li, J. Bao, X. Li, *Acta Physico-Chimica Sinica* 29 (2013) 605.
- [32] S. Salasc, M. Skoglundh, E. Fridell, *Applied Catalysis B* 36 (2002) 145.
- [33] X. Li, Y. Dong, H. Xian, W. Hernández, M. Meng, H. Zou, A. Ma, T. Zhang, Z. Jiang, N. Tsubaki, P. Vernoux, *Energy & Environmental Science* 4 (2011) 3351.
- [34] Q. Ding, H. Xian, Y. Tan, N. Tsubaki, X. Li, *Catalysis Science & Technology* 3 (2013) 1493.
- [35] X. Li, C. Chen, C. Liu, H. Xian, L. Guo, J. Lv, Z. Jiang, P. Vernoux, *ACS Catalysis* 3 (2013) 1071.
- [36] A. Ma, S. Wang, H. Zou, M. Meng, Z. Li, J. Bao, X. Li, *Acta Physico-Chimica Sinica* 28 (2012) 1474.
- [37] S. Rousseau, S. Lorient, P. Delichere, A. Boreave, J.P. Deloume, P. Vernoux, *Applied Catalysis B* 88 (2009) 438.

- [38] M. Couzi, P.V. Huong, *Analytical Chemistry* 9 (1974) 19.
- [39] J.C. Lavalley, *Catalysis Today* 27 (1996) 377.
- [40] I. Rosso, E. Garrone, F. Geobaldo, B. Onida, G. Saracco, V. Specchia, *Applied Catalysis B* 34 (2001) 29.
- [41] D.J. Duvenhage, N.J. Coville, *Applied Catalysis A* 153 (1997) 43.
- [42] D. Ferri, L. Forni, M.A.P. Dekkers, B.E. Nieuwenhuys, *Applied Catalysis B* 16 (1998) 339.
- [43] M.M. Natile, F. Poletto, A. Galenda, A. Glisenti, T. Montini, L. Rogatis, P. Fornasiero, *Chemistry of Materials* 20 (2008) 2314.
- [44] P. Ciambelli, S. Cimino, L. Lisi, M. Faticanti, G. Minelli, I. Pettiti, P. Porta, *Applied Catalysis B* 33 (2001) 193.
- [45] P. Porta, S. Cimino, S. De Rossi, M. Faticanti, G. Minelli, I. Pettiti, *Materials Chemistry and Physics* 71 (2001) 165.
- [46] D.J. Duvenhage, N.J. Coville, *Applied Catalysis A* 233 (2002) 63.
- [47] R. Zhang, A. Villanueva, H. Alamdari, S. Kaliaguine, *Journal of Catalysis* 237 (2006) 368.
- [48] J.N. Kuhn, U.S. Ozkan, *Journal of Catalysis* 253 (2008) 200.
- [49] J. Luo, M. Meng, Y. Zha, Y. Xie, T. Hu, J. Zhang, T. Liu, *Applied Catalysis B* 78 (2008) 38.
- [50] M. Piacentini, M. Maciejewski, A. Baiker, *Applied Catalysis B* 59 (2005) 191.
- [51] S. Kaliaguine, A. Van Neste, V. Szabo, J.E. Gallot, M. Bassir, R. Muzychuk, *Applied Catalysis A* 209 (2001) 345.
- [52] R.Q. Tan, Y.F. Zhu, *Applied Catalysis B* 58 (2005) 61.
- [53] J.F. Moulder, W.F. Stickle, P.E. Sobol, K.D. Bombere, *Handbook of X-ray Photoelectron Spectroscopy*, Perkin-Elmer, Eden Prairie, MN, 1992.
- [54] J. Baltrusaitis, D.M. Cwiertny, V.H. Grassian, *Physical Chemistry Chemical Physics* 9 (2007) 5542.
- [55] A. Galenda, M.M. Natile, V. Krishnan, H. Bertagnolli, A. Glisenti, *Chemistry of Materials* 19 (2007) 2796.
- [56] J. Despres, M. Koebel, O. Kröcher, M. Elsener, A. Wokaun, *Applied Catalysis B* 43 (2003) 389.
- [57] D.H. Kim, J.H. Kwak, J. Szanyi, S.D. Burton, C.H.F. Peden, *Applied Catalysis B* 72 (2007) 233.